Journal of Materials Chemistry A

Accepted Manuscript

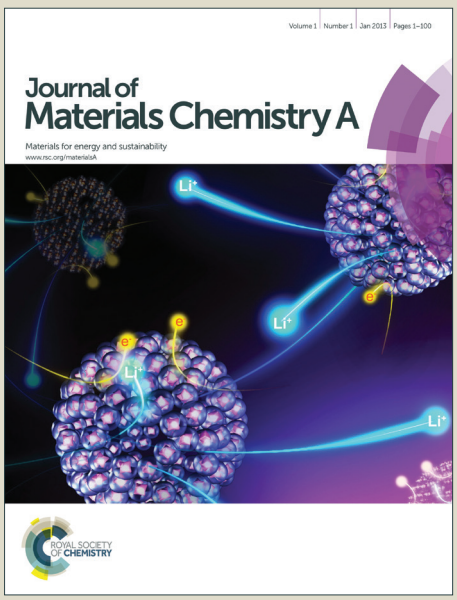

ROYAL SOCIETY OF CHEMISTRY

www.rsc.org/materialsA

Journal of Materials Chemistry A RSCPublishing

ARTICLE

Highly Connected Hierarchical Textured TiO_2 Spheres as Photoanodes for Dye-sensitized Solar Cells

Cite this: DOI: 10.1039/x0xx00000x

Jianjian Lin,[a,b] Andrew Nattestad,*[c] Hua Yu,[b] Yang Bai,[b] Lianzhou Wang,*[b] Shi Xue Dou,[a] Jung Ho Kim,*[a]

Received 00th January 2012,
Accepted 00th January 2012

DOI: 10.1039/x0xx00000x

www.rsc.org/

We present a new type of microstructured TiO_2 sea urchin-like assembly, composed of high aspect-ratio nanosheets. We also demonstrate the applicability of these structures as photoanodes in dye-sensitized solar cells, with 9.0 % conversion efficiency realized, a considerable improvement over commercial Dyesol paste (8.2 %) under the same conditions. We reveal that this new TiO_2 nanostructure is beneficial to enhanced dye loading and efficient light scattering. In particular, the interpenetrating individual sheets of the spheres result in more intimate interparticle connections and provide efficient electron transfer pathways.

Introduction

Dye-sensitized electrochemical photovoltaic cell technology has been recognized as a viable option for power generation.[1] Dye-sensitized Solar Cells (DSCs) have attracted much attention over the past two decades on account of features such as shorter energy pay-back time, lower dependence on the angle of incidence of light, insensitivity to temperature changes, easy fabrication on rigid and flexible substrates, and relatively high energy conversion efficiency.[2-8] One of the core components in the DSC system is usually a wide-band-gap titanium oxide (TiO_2) thin film that serves as a support for the dye molecules and as an electron-transporting medium. Typically, in the photoanode, an insufficient electron diffusion coefficient in electrodes composed of nanometer-sized TiO_2 particles is believed to limit the power conversion efficiency. This is because electron collection is determined by trapping/detrapping events at the sites of the electron traps (defects, surface states, grain boundaries, self-trapping, etc.).[9] With this as the motivation, there is an overwhelming desire among researchers to design and synthesize materials that simultaneously have large surface areas (to absorb more dye molecules), efficient light scattering capability, and faster electron transport. In addition, the pores formed in the TiO_2 layer must be sufficiently large in size, with good connectivity for efficient diffusion of electrolyte components.[10] One solution to this requirement is to use one-dimensional (1D) nanostructures, which can provide direct channels for the rapid collection of the photogenerated electrons, reduce charge recombination, and simultaneously enhance the electrolyte diffusion.[11-15] The typical low surface area of the 1D nanostructures, however, leads to reduced dye loading, and hence reduced light harvesting, resulting in lower photocurrents.

Alternatively, bi-layer structured nanoparticle films have been designed, to confine the incident light within the photoanode.[16-21] Such a configuration, however, increases the thickness of the photoanode film, so that photogenerated electrons at the light scattering layer have to be transported a longer distance within the photoelectrode film to reach the current collector electrode and therefore suffer from a high rate of recombination. Many groups have also tried to combine nanometer-sized particles with micrometer-sized particles to make full use of the combined size advantages.[22-24] Most of these structures, however, were obtained on the basis of separate TiO_2 materials with different morphologies, which unavoidably bring in tedious fabrication procedures.[25]

In this work, we introduce a novel material structure for use in DSC photoanodes, which consists of hierarchical assemblies of polycrystalline anatase TiO_2 nanosheets that appear to resemble sea urchins. These spheres have a bimodal distribution of sizes, leading to both effective dye adsorption and effective light-scattering behaviour, as well as enhanced electronic interconnectivity within the photoanode. An overall energy conversion efficiency of up to 9.0 % can be achieved by using these highly connected hierarchical textured TiO_2 spheres (HCHT) as the photoelectrode with N719 dye.

Results and discussion

HCHT were synthesized by hydrothermal treatment of a solution of titanium butoxide (TB) and acetic acid (HAc), which was followed subsequently by calcination at 500 °C. Fig. 1(a, c) shows scanning electron microscope (SEM) images of the final product. The thin two-dimensional (2D) nanosheets can be seen to be the primary building units of these larger structures, with an average thickness of approximately 10 nm. These can be more clearly distinguished in Fig. 1(d) and Fig. S1(c), where they are assembled into hierarchical spheres, in the Supporting Information (SI). Interestingly, the size distribution in Fig. 1(b) reveals a bimodal distribution centered at ~ 0.4 and 2.0 μm. Kuang's group could obtain different morphologies and sizes by adjusting hydrothermal conditions, such as precursor concentrations or reaction temperature.[26-27] The microstructure of the hierarchical spheres was directly observed by transmission electron microscopy (TEM). In the higher resolution images in Fig. 1(e, f), it can be seen that the nanosheets are perpendicular to the sphere surface and are interlocked with the nanosheets of neighbouring spheres. The small features, created by these sheets, also allow for high dye loading, a feature typically counterposed to effective light scattering. The high resolution TEM (HRTEM) image [Fig. 1(g)] confirms that the calcined hierarchical TiO_2 spheres are composed of crystalline TiO_2 nanocrystals with a fringe spacing of approximately 3.5 Å, corresponding to the (101) plane of anatase phase. The related selected area electron diffraction (SAED) pattern in Fig. 1(d) also confirms the polycrystalline nature of the hierarchical spheres, with the three most distinct concentric diffraction rings, moving outward from the centre, assigned to the (101), (103), and (200) planes of anatase TiO_2, respectively. In addition, the successful preparation of anatase is further demonstrated by the X-ray diffraction (XRD) pattern [Fig. 1(h)] and the Raman spectrum [Fig. S1(e)].

The formation mechanism of such a nanosheet-based hierarchical structure can be understood by examining precipitates extracted at different stages of the reaction, as shown in Scheme 1. Based on TEM (Fig. S2), XRD (Fig. S3), and Fourier transform infrared spectroscopy (FTIR) characterizations (Fig. S4), it can be determined that HAc does not fully react with TB during a short reaction time such as 1 h, and the sample features agglomerated nanocrystals [Fig. S2(a)]. The presence of the asymmetric and symmetric stretching vibrations of the carboxylic groups centered at 1566, 1452, and 1421 cm^{-1} [Fig. S4(b)] reveals the coordination of

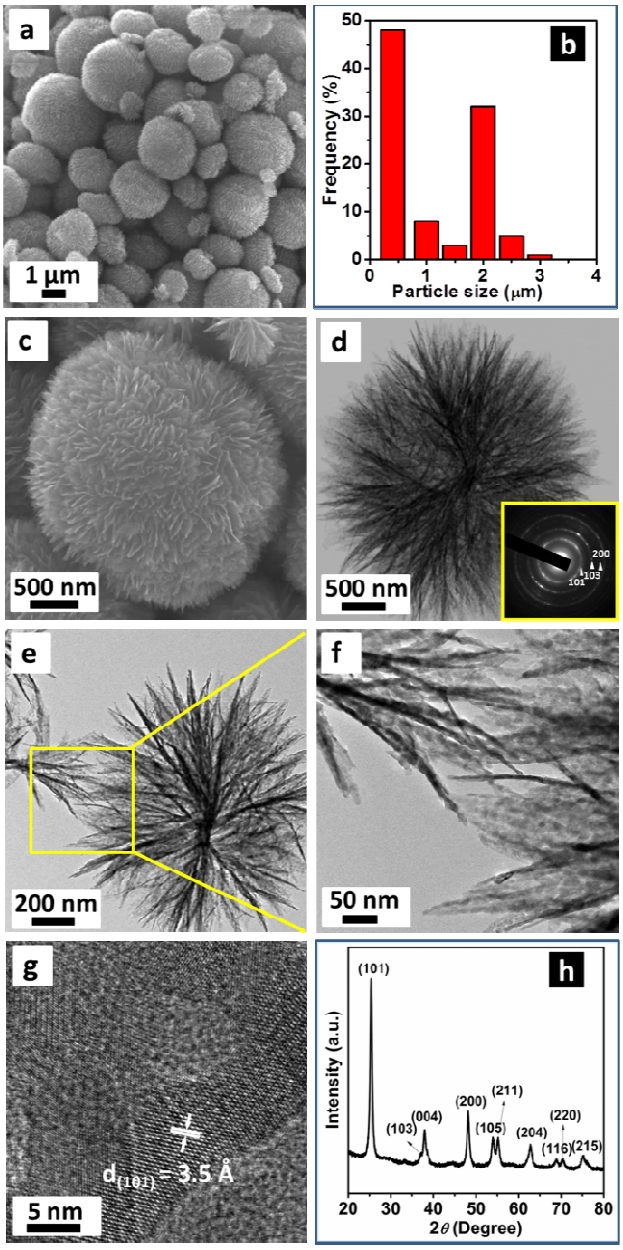

Fig. 1 Physical characterization of the calcined HCHT: (a) low magnification SEM image; (b) particle size distribution, based on 600 particles from Fig. S1(a) using Image J software; (c) SEM image of an individual sphere; (d) bright-field TEM image visualizing the nanosheet building blocks, with inset: selected area electron diffraction (SAED) pattern of the whole sphere in (d); (e) TEM image of two typical interconnected spheres; (f) enlarged TEM image revealing details of the interconnection of nanosheets; (g) HRTEM image showing the fringe spacing of anatase TiO_2 nanocrystals; and (h) XRD pattern of the calcined HCHT, indicating TiO_2 crystals with the tetragonal anatase phase (JCPDS No. 21-1272, a = 3.785 Å, b = 3.785 Å, c = 9.514 Å) after the calcination treatment, without any impurity phase.

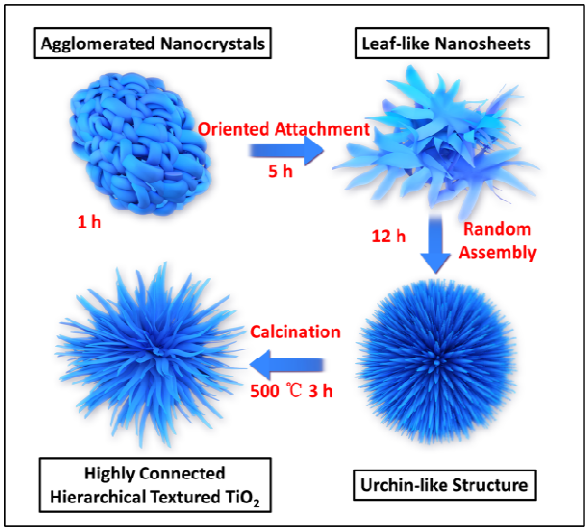

Scheme 1. Schematic diagram of the formation process of HCHT.

HAc to the titanium centres,[28, 29] indicating the formation of a titanium-containing intermediate (Fig. S3). With an extended reaction time (5 h), the Ti-complex intermediates assembled to form leaf-like nanosheets through an oriented attachment process, to bear some resemblance to the HCHT particles [Fig. S2(b)]. This was, however, only seen to be fully complete after 12 h, with urchin-like structures appearing [Fig. S2(c)]. It should be noted that XRD of these structures (Fig. S3) reveals that this material still has low crystallinity. Calcination is required to obtain the highly crystalline material, from the decomposition of the as-prepared Ti-complex intermediate spheres to TiO_2.

The formation of the leaf-like nanosheets is concluded to occur via the following mechanism of acidolysis of TB, catalyzed by HAc through the formation of a Ti-acetate complex. Evidence of this TB-HAc complex is seen with FTIR [Fig. S4(a, b)],[30] with a weak band at 1721 cm^{-1} corresponding to the stretching vibration of the C=O group of HAc. In comparison with pure TB and HAc, new bands are observed at 3426, 1566, 1452, 1421, and 1259 cm^{-1}. It is well known that acetate ligands are produced by the reaction of TB with HAc and have several modes of coordination, including monodentate and bidentate (chelating and bridging).[31-33] The alcohol nC_4H_9OH is also generated as a by-product in the formation process of these acetate ligands. The peak at 3426 cm^{-1}, (observed for all intermediates), should be assigned to the stretching vibration of the hydroxyl groups on nC_4H_9OH.[34] Moreover, the separation ($\Delta\nu$ = 140 cm^{-1}) between 1566 and 1426 cm^{-1} suggests that some acetate groups act as bridging ligands between two titanium atoms.[31-33] The presence of the 1721 cm^{-1} (C=O) band can be attributed to the contribution of monodentate-coordinated acetates, while the weak absorption indicates the small amount of such monodentate-coordinated acetates, so that, it can be concluded that most of the Ti-acetate complexes are bidentate-coordinated acetates. Through the acidolysis process, the nascent TiO_2 nanocrystals are surrounded by numerous bidentate-coordinated acetates. Given the direction of the π-π interactions, amorphous leaf-like nanosheets are constructed by the oriented aggregation of these TiO_2 nanocrystals.[30] In addition, thermogravimetric analysis (TGA) of the as-prepared precipitates, measured under flowing air (Fig. S5), indicated that a considerable amount of nC_4H_9OH (~ 29 wt%) was trapped inside the Ti-complex intermediate spheres, and the complete decomposition of the organics occurred at approximately 400 ºC.[31] Above 400 ºC, the weight of the sample remains almost constant. The sharp peak in the differential scanning calorimetry (Fig. S5) curve, starting at approximate 350 ºC, corresponds to the crystallization of the amorphous residue into anatase. Finally, calcination at 500 ºC for 3 h resulted in the formation of pure HCHT, as shown in Fig. 1.

Nitrogen adsorption-desorption measurements were performed to obtain the Brunauer-Emmett-Teller (BET) specific surface area, porosity, and pore size distribution for state-of-the-art commercial TiO_2 screen printing pastes [18NR-T Transparent Titania Paste" (hereafter, Dyesol-T) and WER2-O Reflector Titania Paste (hereafter, Dyesol-S), obtained from Dyesol (Australia)], and HCHT materials. As observed in Fig. 2(a), the isotherm of the HCHT appears to be a Type IV curve with an H3 hysteresis, which is usually ascribed to slit-like mesopores formed by sheet-like particles.[35] The two hysteresis loops in the isotherm suggest that

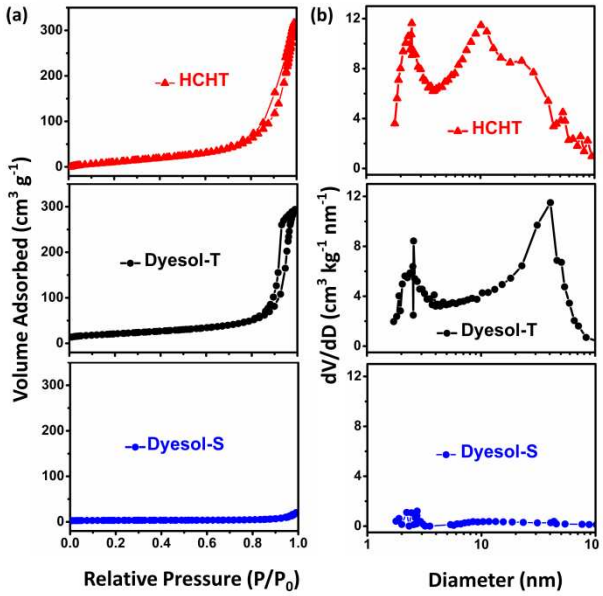

Fig. 2. (a) N_2 adsorption-desorption isotherms of the HCHT (red closed triangles), the Dyesol-transparent layer (Dyesol-T, 18NR-T, black closed circles) and the Dyesol-scattering layer (Dyesol-S, WER2-O, blue closed circles); and (b) corresponding pore size distributions calculated by the BJH method from the adsorption branch. Before BET measurements, all the particles were dried and then calcined at 500 ºC for 3 h.

hierarchical nanoporous structures exist within the matrix, which can be directly verified by the pore size distribution plot in Fig. 2(b) [determined by Barrett-Joyner-Halenda (BJH) analysis]. The pore size distribution of the HCHT ranges between 2 and 100 nm, with a bimodal pore size distribution centered at 2.5 nm and 10 nm (as might be expected given the hierarchical structure). Interestingly, the mean average pore diameter is 17.6 nm due to large mesopores with diameters of more than 10 nm, accounting for the majority of the slit-like mesopores, which result from the gaps between the randomly assembled nanosheets and can be seen clearly in Fig. S1(b).[36] In addition, the voids formed by aggregated spheres may also contribute to the large pores [Fig. 1(a)].[37] It is well known that for good performance the pores formed in the TiO_2 layer must be sufficiently large in size with excellent mutual connectivity for the efficient diffusion of electrolyte;[10] As such, larger pores (between spheres) in HCHT can serve as "highways" for efficient electrolyte diffusion. The data on the BET specific surface areas, porosities, and

Table 1 Specific surface area, porosity, and roughness factor of Dyesol and HCHT materials.

Samples	Specific surface area (m^2 g^{-1})	Porosity[a)] (%)	Roughness factor[b)] (μm^{-1})
Dyesol-S	10	9.82	35.2
Dyesol-T	74	64.2	103.3
HCHT	103	66.9	133.0

[a)] The porosities (*P*) of Dyesol-S, Dyesol-T and HCHT were calculated according to: $P=V_p/(\rho^{-1} + V_p)$, where V_p is the specific cumulative pore volume (cm^3 g^{-1}) and ρ^{-1} is the inverse of the density of anatase TiO_2 (ρ^{-1} = 0.257 cm^3 g^{-1}).[38]

[b)] An estimation of the roughness factor (*R*) per unit film thickness of the films is obtained by $R = \rho(1-P)S$, where ρ is the density (g cm^{-3}) of anatase TiO_2, *P* is the porosity (%) of the film, and *S* is the specific surface area(m^2 g^{-1}).[39]

roughness factors for the Dyesol-S, Dyesol-T, and HCHT are summarized in Table 1. The data show that the HCHT film has a larger surface area and higher porosity than the Dyesol film, indicating that HCHT have higher dye adsorption capability. The approximately 1.3 times higher roughness factor in the HCHT film leads to an increase in the light harvesting efficiency due to the larger amount of dye adsorption, which will be further discussed below.

The HCHT were applied in photoanodes of DSCs. The thickness of the film derived from the spheres was around 15 µm. The morphology of the spherical TiO_2 structures is clearly seen in the film prepared from HCHT [shown in the inset of Fig. 3 and Fig. S6(a)]. For comparison, a Dyesol-based film with a double layer [12 µm transparent layer (Dyesol-T) + 4 µm scattering layer (Dyesol-S)] was prepared under analogous conditions (refer to Experimental section at the end of this paper). Fig. 3 shows the current density-voltage (*J-V*) characteristics of the Dyesol-based and HCHT-based DSCs. As listed in Table 2, the Dyesol-based DSCs showed an open-circuit photovoltage (V_{oc}) of 0.805 V, a short-circuit photocurrent density (J_{sc}) of 14.3 mA cm^{-2}, and an energy conversion efficiency (η) of 8.2 %, while the HCHT-based DSCs showed a V_{oc} of 0.850 V, a J_{sc} of 17.1 mA cm^{-2}, and an η of 9.0 % under one sun conditions, resulting in a 19.6 % and 6 % increase in J_{sc} and V_{oc}, respectively. The remarkable increase in J_{sc} is probably attributable to the larger surface area due to the hierarchical and mesoporous morphology of the HCHT photoanode, allowing it to take up more dye molecules (5.9×10^{-7} mol cm^{-2}), in tandem with light scattering (discussed in more detail below).

To quantify the dye loading, N719 stained films were exposed to a 0.1 M NaOH solution and the amount of desorbed dye molecules was examined by ultraviolet-visible (UV-Vis) spectroscopy [shown in Fig. S6(b)]. The absorption spectrum of the desorbed dye represents the amount of dye adsorbed at the photoanode. The two spectra show two peaks at 378 nm and 512 nm which are blue-shifted from the original N719 dye absorption peaks, as typically occurs in alkaline solutions.[40] In general, as the amount of dye adsorption increases, more light can be harvested, so that

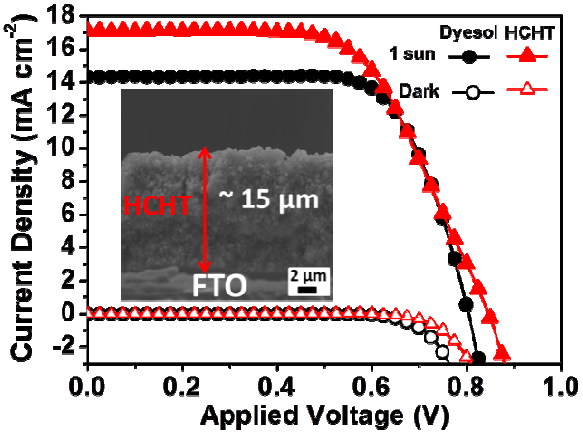

Fig. 3. *J-V* characteristics of Dyesol- and HCHT-based DSCs. Illumination intensity of 100 mW cm^{-2} with AM 1.5 and active area of 0.16 cm^2 were applied. Inset is a SEM cross-sectional image of the nanosheet-based highly connected hierarchical anatase TiO_2 sphere film on the fluorine-doped tin oxide (FTO) layer, with the film applied by the doctor blade method.

Table 2 Photovoltaic parameters of cells based on Dyesol and HCHT photoanodes measured under air mass (AM) 1.5 global (1.5G) one sun illumination (100 mW cm^{-2}). J_{sc}: short-circuit photocurrent density; V_{oc}: open-circuit photovoltage; *FF*: fill factor; η: total power conversion efficiency. The active areas were ~ 0.16 cm^2 for all of the cells (with the mask area 0.25 cm^2), and the data presented are average values obtained after testing four cells.

Samples	J_{sc} (mA cm^{-2})	V_{oc} (V)	*FF* (%)	η (%)	Amount of dye[a] (10^{-7} mol cm^{-2})	Film thickness[b] (µm)
Dyesol	14.3 ± 0.2	0.805 ± 0.01	71.0 ± 2	8.2 ± 0.2	3.7	16 ± 0.3
HCHT	17.1 ± 0.5	0.850 ± 0.02	62.0 ± 2	9.0 ± 0.2	5.9	15 ± 0.5

[a] The dyed electrodes were soaked in a 0.1 M alkaline solution in ethanol and water to desorb the dye from the electrodes. The amount of desorbed dye was quantified by measuring its optical absorption spectrum.
[b] Measurement of film thickness was carried out on a surface profile system (Veeco Dektak 150).

there is a larger photocurrent density.[41] The amount of adsorbed dye for the HCHT photoanode (5.9×10^{-7} mol cm^{-2}) is significantly higher than for the Dyesol photoanode (3.7×10^{-7} mol cm^{-2}), which may contribute to the remarkably improved J_{sc} for the HCHT-based DSCs.

Even if the dark current cannot be directly related to the back electron transfer process, since the electrolyte concentration in the films and the potential distribution across the nanoporous electrode in dark current are different from those under illumination, it has been considered as a qualitative technique to describe the extent of the back electron transfer.[42] Furthermore, dark *J-V* curves show the dark current onset of the HCHT-based DSC has shifted to a higher potential, and a smaller dark current is produced at the same potential above 0.7 V. These observations indicate a lower recombination rate between transferred electrons and I_3^- ions for the HCHT.

To investigate the scattering efficiency of the Dyesol and HCHT films, the reflectivity of each film was studied. The inset in Fig. 4 shows the diffuse reflectance spectra of the Dyesol film and the HCHT film. Both films show highly diffuse reflection capability across most of the visible spectrum. Diffuse reflectivity is observed to be lower for the Dyesol film for wavelengths from 400 nm to 800 nm. It is worth noting that from 600 nm to 800 nm, which is actually the region in which diffuse reflectivity is most critical, as the extinction co-efficient of the dye (N719) is comparatively low. The HCHT film scattered this light more effectively, which gave it a higher probability of being absorbed. Films produced from the HCHT show superior diffuse reflection capabilities for longer wavelengths (600–800 nm) due to the larger particle size, which is comparable to the wavelength of the incident light in question.

Fig. 4 displays the wavelength distribution of the incident monochromatic photon to current conversion efficiency (IPCE) for both the Dyesol and the HCHT films. The IPCE is determined by the light absorption efficiency of the dye, the quantum yield of electron injection, and the efficiency with which electrons are collected at the conducting glass substrate, which is strongly affected by the morphology and surface area of the photoelectrode. Both films result

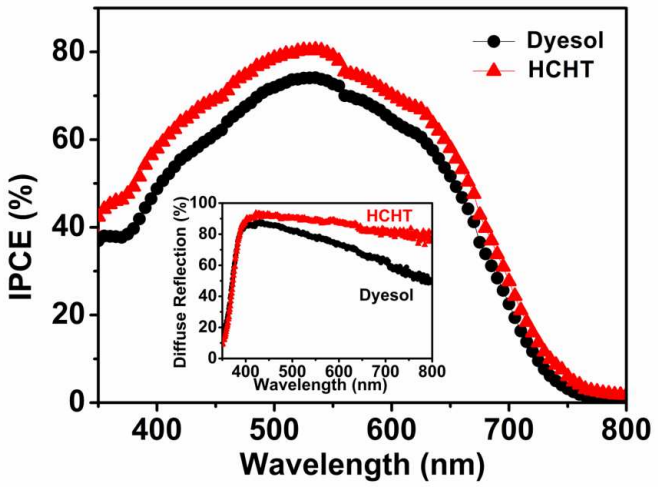

Fig. 4. Incident photon to current conversion efficiency (IPCE) curves of Dyesol-based (12 μm transparent layer + 4 μm scattering layer film) and HCHT-based (15 μm film) DSCs; inset: diffuse reflectance spectra of the Dyesol and HCHT films.

in reasonably broad IPCE response, with the HCHT film giving a higher response across the whole spectrum. Closer analysis (Fig. S7) reveals the enhancement in IPCE to be most marked at $\lambda > 650$ nm. In the short-wavelength spectral region (400-450 nm), the IPCE of the Dyesol film is about 8 % lower than that of the HCHT film. In this spectral region, iodide species (I_3^-) in the electrolyte absorb strongly, in conjunction with the lower dye loading absorbed, attenuating the amount of light reaching the sensitizing dye and thus limiting the photocurrent. At the maximum value of the IPCE spectra at 535 nm, the IPCE of the HCHT film is approximately 6 % higher than that of the Dyesol film.

In order to study the interfacial reactions of photoexcited electrons and better understand the kinetics of electrochemical and photoelectrochemical processes occurring in DSC operations, electrochemical impedance spectroscopy (EIS) was performed.[43-46] Fig. 5(a) presents the Nyquist plots of the impedance spectra obtained under one sun illumination for DSCs assembled with the Dyesol and HCHT films under V_{oc}. The equivalent circuit is shown as the inset and the fitting data are given in Fig. S8 and Table S1. In general, three semicircles extending from the total series resistance (R_s) can be recognized and fitted according to an equivalent circuit model, where the finite diffusion element is also represented by the shunt resistance and low frequency constant phase element (CPE). The semicircle in the high frequency region represents the impedance corresponding to charge transfer at the counter electrode (R_{ct1}), while those at intermediate frequency and low-frequency give information on the impedance at the TiO_2/electrolyte interface (R_{ct2}), related to the charge transport/recombination, and the finite diffusion of the electrolyte (R_{diff}), respectively.[44, 46-48] According to the approach of Adachi *et al.*,[49] several parameters related to the properties of electron transport in the semiconductor can be deduced from the Nyquist plot. In particular, the charge transfer (recombination) resistance (R_{ct2}) related to electron-hole recombination can be determined from the central arc diameter. In our case, it was found that the recombination resistance at the TiO_2/dye/electrolyte interface (R_{ct2}) for HCHT was smaller than for the devices made using the commercial paste, which indicates that electrons are easier to move at the HCHT surface and contribute to the charge transport at the photoanode. The Bode phase plots shown in Fig. 5(b) likewise support the differences in the electron lifetime for the TiO_2 films derived from Dyesol and HCHT. Three main frequency peaks are observed. These peaks correspond to the charge transfer processes at different interfaces within the DSCs. Interestingly, the maximum frequency in the intermediate frequency regime, which is related to electron transfer in the HCHT-based film, is lower than that for the Dyesol-based film. According to the EIS model developed by Kern *et al.*,[50] the electron lifetime (τ_{eff}) of injected electrons in a TiO_2 film can be calculated from the low frequency results as:

$$\tau_{\text{eff}} = \frac{1}{2\pi f_{\text{max}}} \qquad (1)$$

where the characteristic f_{max} is the maximum frequency in the mid-frequency peak. The middle-frequency peak of the Dyesol particle containing DSC is at a higher frequency (50.22 Hz) compared to the

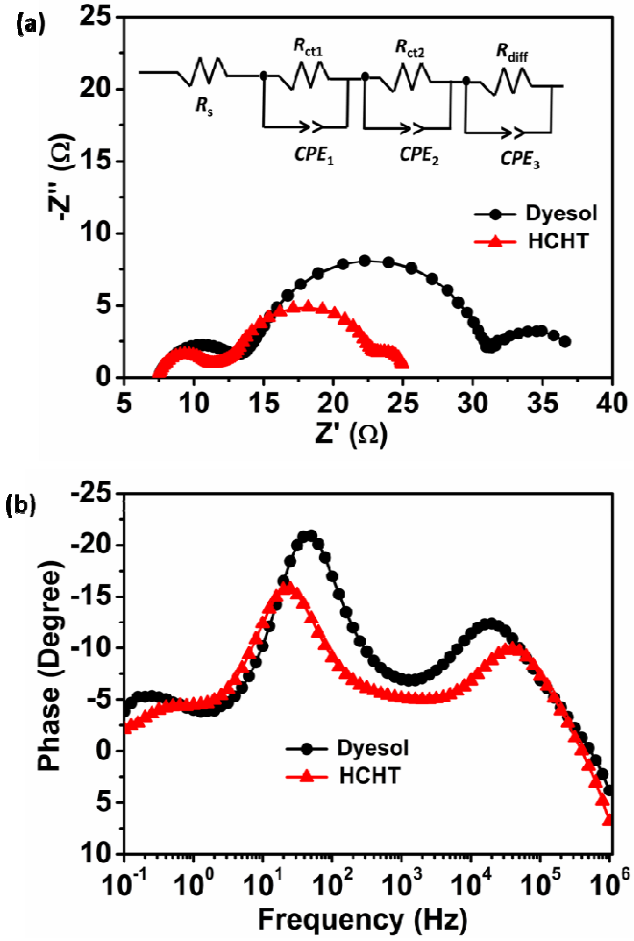

Fig. 5 Impedance spectra of DSCs containing Dyesol and HCHT photoanodes measured at V_{oc} under illumination of 100 mW cm^{-2}: (a) Nyquist plots, with the inset showing the equivalent circuit, and (b) Bode phase plots.

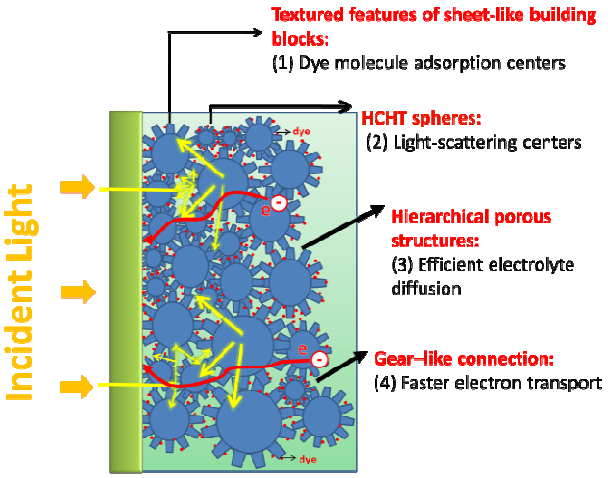

Scheme 2 Schematic illustration of photoanode structure with four functions.

HCHT-based DSC (24.93 Hz), indicating a longer lifetime (6.4 ms) for the HCHT (3.2 ms for the Dyesol). Longer electron lifetimes are observed for HCHT-sensitized solar cells, indicating more effective suppression of the back-reaction of the injected electrons with the I_3^- ions in the electrolyte.

To summarize, based on the above characterizations, HCHT particles have several functions particularly well suited for application in DSCs. This is shown in Scheme 2. The sheet-like building blocks result in a high active surface area, which, in turn, allows for improved dye loading. Concurrently the spheres formed by these sheets are effective light-scattering centres across a broad range of incident wavelengths. Because of the bimodal pore size distributions, the large external pores can serve as "highways" for efficient electrolyte diffusion. Finally, the overlapping and interconnected 2D nansheets provide improved conduction pathways for electron transfer.

Conclusions

A new type of highly connected hierarchical textured TiO_2 spheres (HCHT) was successfully synthesized by a facile hydrothermal process. The HCHT with well-defined mesopores simultaneously possess high specific surface area, a pronounced light-scattering effect (especially for $\lambda > 600$ nm), and fast electron transport. The DSCs made from HCHT exhibit higher energy conversion efficiency of 9.0 %, compared to 8.2 % for the commercial Dyesol TiO_2 double layer photoanode.

Experimental

Synthesis of Highly Connected Hierarchical Textured TiO_2 Spheres (HCHT)

Acetic acid (HAc, ACS reagent, ≥ 99.7 %) and titanium butoxide (TB, Ti $(OCH_2CH_2CH_2CH_3)_4$, 97 %, analytical reagent) were purchased from Sigma-Aldrich, and used without further purification. The fabrication of HCHT from a TB-HAc solution was simply obtained by a hydrothermal approach. In detail, 0.5 mL of TB was added into 30 mL of HAc solution under magnetic stirring and kept for 1 h at room temperature, before being transferred to a Teflon-lined stainless steel pressure vessel (45 mL capacity, Parr Instrument Company) and heated in oven to 150 °C for 12 h (heating ramp rate of 1 °C min^{-1}). After the autoclave cooled down to room temperature, the product was collected by centrifugation, washed with distilled water and ethanol several times, dried at 90 °C overnight, and calcined at 500 °C for 3 h to remove the residual organics.

Preparation of TiO_2 Photoanodes

To prepare the DSC working electrodes, fluorine doped tin oxide (FTO) glass as current collector (2.3 mm thickness, 8 Ω/sq, Hartford Glass) was first cleaned with soapy water for 20 min and rinsed with distilled water, then soaked in acetone and then ethanol in an ultrasonic bath for 30 min. Firstly, the blocking layer solution was created by diluting titanium diisopropoxide bis(acetylacetonate), 75 % in isopropanol (Aldrich, 32525-2), in absolute ethanol in the volume ratio of 1:9. After drying in nitrogen, the blocking layer was deposited on the clean FTO glass by spray pyrolysis. Then, a layer of TiO_2 paste was cast onto the FTO glass plates by the doctor-blade method. The paste fabrication process is as follows: briefly, TiO_2 powders (1.0 g) were ground in a mixture of ethanol (20 mL), distilled water (0.833 mL), acetic acid (0.167 mL), terpineol (4 g), and ethyl cellulose (0.5 g) to form a slurry, and then the slurry was sonicated for 1 h in an ultrasonic bath and stirred for 1 h. A viscous white TiO_2 paste was finally obtained after an evaporation process. After a heating process (at 150 °C for 10 min, at 325 °C for 5 min, at 375 °C for 5 min, at 450 °C for 30 min, and then at 500 °C for 15 min) to remove organic substances, the TiO_2 films were soaked in 0.02 M aqueous titanium tetrachloride solution ($TiCl_4$) at 70 °C for 30 min. As a final step, the films were washed with water, and then ethanol, dried, and sintered again (500 °C for 30 min). Before the TiO_2 paste was cast onto the FTO glass, a single blocking layer [with the solution created by diluting titanium diisopropoxide bis (acetylacetonate), 75 % in isopropanol (Aldrich, 32525-2), in absolute ethanol with volume ratio 1:9] was deposited on FTO glass by the pyrolysis method.

Fabrication of Dye-Sensitized Solar Cells

The resultant TiO_2 films were immersed in a 0.5 mM N719 (Solaronix) dye solution in a 1:1 (v/v) mixture of acetonitrile (HPLC, Lab-scan) and *tert*-butanol (LR, Ajax Chemicals) for about 24 h once the temperature had decreased to approximately 110 °C. After dyeing, the samples were taken out of the dye bath, washed with acetonitrile, and dried. The Pt counter electrode was produced using a pre-drilled piece of 2.3 mm FTO glass, coated with one drop of 10 mM platinic acid solution (H_2PtCl_6) and heated to 400 °C for 20 min. The working electrode and Pt counter electrode were assembled into a sandwich type cell and sealed with a spacer of 25 µm Surlyn (Solaronix). An I^-/I_3^- organic solvent based electrolyte solution [85:15 vol % of acetonitrile/valeronitrile, 0.03 M iodine (I_2), 0.5 M 4 tertbutylpyridine (4-tBP), 0.6 M 1-butyl-3-

methylimidazolium iodide (BMII), and 0.1 M guanidinium thiocyanate (GuSCN)] was introduced via vacuum back-filling. The hole was sealed using another piece of aluminium-backed Surlyn.

Characterizations

The crystalline structure of the samples was characterized by using a Bruker Advance X-Ray Diffractometer (40 kV, 30 mA) with Cu Kα (λ = 0.15406 nm) radiation at a scan rate of 1° /min from 5º to 80º (2θ). The morphology of the samples was examined by scanning electron microscopy (SEM, JEOL 7001) and transmission electron microscopy (TEM, JEM-2100F). Brunauer–Emmett–Teller (BET) surface areas (S_{BET}) were determined by using a nitrogen adsorption apparatus (Tristar 3030, Micromeritics Instrument Corporation). All samples were degassed at 150 °C overnight before measurement. Dye desorption was performed by dipping the sensitized sample into 0.1 M NaOH in ethanol-water (1:1) solution. The effective dye loading was determined from the absorption value for each NaOH/dye solution according to Beer's law. The light absorption and scattering properties of the samples were investigated by ultraviolet (UV)-visible light absorption/diffuse reflectance spectrometry (Shimadzu UV-3600). Thermogravimetric (TG) and differential thermal analysis (DTA) were carried out on a Mettler Toledo GC200 instrument from 25 to 600 °C with a heating rate of 3 °C min^{-1}. Film thickness was measured with a Veeco Dektak 150 Surface Profiler. Photocurrent density – voltage (J–V) curves were measured using a Keithley 2400 sourcemeter, a simulated 100 mW cm^{-2} air mass (AM) 1.5 light source (Oriel), and customized LabView software. The device area was masked with a metallic mask slightly larger than the active area. The intensity was adjusted to give 100 mW cm^{-2} on a calibrated Si photodiode (PECCELL) equipped with a cut-off filter giving a spectral response similar to N719. Incident photon-to-current quantum conversion efficiency (IPCE) was measured using a 300 W Xe lamp, a monocromator with sorting filters focused on a spot with additional optics. The short circuit current response of the devices was recorded in 5 nm steps using a Keithley 2400 SMU. The measured currents were referenced to a calibrated Si photodiode (PECCELL).

Acknowledgements

The work is supported by an Australian Research Council Discovery Projects (DP1096546 and DP130102905). Dr. Andrew Nattestad would like to thank the Australian Renewable Energy Agency (ARENA) for financial support. The authors would also like to thank the Australian National Fabrication Facility (ANFF) for access to equipment. The authors would like to also thank Dr. Tania Silver for critical reading of the manuscript.

Notes and references

[a] Institute for Superconducting and Electronic Materials (ISEM), Australian Institute for Innovative Materials (AIIM), University of Wollongong, NSW 2522, Australia. E-mail: jhk@uow.edu.au

[b] Nanomaterials Centre, School of Chemical Engineering and Australian Institute for Bioengineering and Nanotechnology, The University of Queensland, Brisbane, QLD 4072, Australia. E-mail: l.wang@uq.edu.au

[c] Intelligent Polymer Research Institute, ARC Centre of Excellent for Electromaterials Science, AIIM, University of Wollongong, NSW 2522, Australia. E-mail: anattest@uow.edu.au

1. M. Gratzel, *Nature*, 2001, **414**, 338-344.
2. B. Oregan and M. Gratzel, *Nature*, 1991, **353**, 737-740.
3. Z. B. Yang, T. Chen, R. X. He, G. Z. Guan, H. P. Li, L. B. Qiu and H. S. Peng, *Adv. Mater.*, 2011, **23**, 5436-5439.
4. A. Yella, H. W. Lee, H. N. Tsao, C. Y. Yi, A. K. Chandiran, M. K. Nazeeruddin, E. W. G. Diau, C. Y. Yeh, S. M. Zakeeruddin and M. Gratzel, *Science*, 2011, **334**, 629-634.
5. T. Chen, L. B. Qiu, H. G. Kia, Z. B. Yang, and H. S. Peng, *Adv.Mater.*, 2012, **24**, 4623-4628.
6. H. S. Kim, C. R. Lee, J. H. Im, K. B. Lee, T. Moehl, A. Marchioro, S. J. Moon, R. Humphry-Baker, J. H. Yum, J. E. Moser, M. Gratzel and N. G. Park, *Sci. Rep.*, 2012, **2**. 591.
7. J. Burschka, N. Pellet, S. J. Moon, R. Humphry-Baker, P. Gao, M. K. Nazeeruddin and M. Gratzel, *Nature*, 2013, **499**, 316-319.
8. S. W. Pan, Z. B. Yang, H. P. Li, L. B. Qiu, H. Sun and H. S. Peng, *J. Am. Chem. Soc.*,2013, **135**, 10622-10625.
9. Y. C. Park, Y. J. Chang, B. G. Kum, E. H. Kong, J. Y. Son, Y. S. Kwon, T. Park and H. M. Jang, *J. Mater. Chem.*, 2011, **21**, 9582-9586.
10. Y. J. Kim, M. H. Lee, H. J. Kim, G. Lim, Y. S. Choi, N.-G. Park, K. Kim and W. I. Lee, *Adv. Mater.*, 2009, **21**, 3668-3673.
11. K. Zhu, N. R. Neale, A. Miedaner and A. J. Frank, *Nano Lett.*, 2007, **7**, 69-74.
12. G. K. Mor, K. Shankar, M. Paulose, O. K. Varghese and C. A. Grimes, *Nano Lett.*, 2006, **6**, 215-218.
13. C. Y. Lin, Y. H. Lai, H. W. Chen, J. G. Chen, C. W. Kung, R. Vittal and K. C. Ho, *Energy Environ. Sci.*, 2011, **4**, 3448-3455.
14. Y. L. Wang, M. Guo, M. Zhang and X. D. Wang, *CrystEngComm*, 2010, **12**, 4024-4027.
15. M. Law, L. E. Greene, J. C. Johnson, R. Saykally and P. Yang, *Nat. Mater.*, 2005, **4**, 455-459.
16. S. Ito, T. N. Murakami, P. Comte, P. Liska, C. Gratzel, M. K. Nazeeruddin and M. Gratzel, *Thin Solid Films*, 2008, **516**, 4613-4619.
17. X. H. Miao, K. Pan, Y. P. Liao, W. Zhou, Q. J. Pan, G. H. Tian and G. F. Wang, *J. Mater. Chem. A*, 2013, **1**, 9853-9861.
18. X. H. Sun, Y. M. Liu, Q. D. Tai, B. L. Chen, T. Peng, N. Huang, S. Xu, T. Y. Peng and X. Z. Zhao, *J. Phys. Chem. C*, 2012, **116**, 11859-11866.
19. Z. P. Zhang, S. Ito, B. O'Regan, D. B. Kuang, S. M. Zakeeruddin, P. Liska, R. Charvet, P. Comte, M. K. Nazeeruddin, P. Pechy, R. Humphry-Baker, T. Koyanagi, T. Mizuno and M. Gratzel, *Z. Phys. Chemie-Int. J. Res. Phys. Chem. Chem. Phys.*, 2007, **221**, 319-327.
20. L. Zhao, J. Li, Y. Shi, S. M. Wang, J. H. Hu, B. H. Dong, H. B. Lu and P. Wang, *J. Alloy. Compd.*, 2013, **575**, 168-173.
21. X. Wu, G. Q. Lu and L. Z. Wang, *Energy Environ. Sci.*, 2011, **4**, 3565-3572.
22. Z. S. Wang, H. Kawauchi, T. Kashima and H. Arakawa, *Coord. Chem. Rev.*, 2004, **248**, 1381-1389.
23. C. J. Barbe, F. Arendse, P. Comte, M. Jirousek, F. Lenzmann, V. Shklover and M. Gratzel, *J. Am. Ceram. Soc.*, 1997, **80**, 3157-3171.
24. L. Yang, Y. Lin, J. G. Jia, X. R. Xiao, X. P. Li and X. W. Zhou, *J. Power Sources*, 2008, **182**, 370-376.
25. V. Suryanarayanan, K. M. Lee, J. G. Chen and K. C. Ho, *J. Electroanal. Chem.*, 2009, **633**, 146-152.
26. J. Y. Liao, B. X. Lei, D. B. Kuang and C. Y. Su, *Energy Environ. Sci.*, 2011, **4**, 4079-4085.
27. J. Y. Liao, J. W. He, H. Y. Xu, D. B. Kuang and C. Y. Su, *J. Mater. Chem.*, 2012, **22**, 7910-7918.
28. Z. H. Zhang, X. H. Zhong, S. H. Liu, D. F. Li and M. Y. Han, *Angew. Chem., Int. Ed.*, 2005, **44**, 3466-3470.
29. D. Jiang, Y. Xu, B. Hou, D. Wu and Y. H. Sun, *Eur. J. Inorg. Chem.*, 2008, **8**, 1236-1240.
30. L. Li and C.-y. Liu, *CrystEngComm*, 2010, **12**, 2073-2078.

31. S. Doeuff, M. Henry, C. Sanchez and J. Livage, *J. Non-Cryst. Solids.*, 1987, **89**, 206-216.
32. J. C. S. Wu, I. H. Teseng and W. C. Chang, *J. Nanopart. Res.*, 2001, **3**, 113-118.
33. Z. Zhang, X. Zhong, S. Liu, D. Li and M. Han, *Angew. Chem., Int. Ed*., 2005, **44**, 3466-3470.
34. U. Hwang, H. Park and K. Koo, *Ind. Eng. Chem. Res.*, 2004, **43**, 728-734.
35. M. Kruk and M. Jaroniec, *Chem. Mat.*, 2001, **13**, 3169-3183.
36. W. Yang, J. Li, Y. Wang, F. Zhu, W. Shi, F. Wan and D. Xu, *Chem. Commun.*, 2011, **47**, 1809-1811.
37. J. Jiang, F. Gu, W. Shao and C. Z. Li, *Ind. Eng. Chem. Res.*, 2012, **51**, 2838-2845.
38. J. van de Lagemaat, K. D. Benkstein and A. J. Frank, *J. Phys. Chem. B*, 2001, **105**, 12433-12436.
39. K. D. Benkstein, N. Kopidakis, J. van de Lagemaat, A. J. Frank, *J. Phys. Chem. B,* 2003, **107**, 7759-7767.
40. E. Palomares, R. Vilar and J. R. Durrant, *Chem. Commun.*, 2004, **10**, 362-363.
41. G. Schlichthorl, S. Y. Huang, J. Sprague and A. J. Frank, *J. Phys. Chem. B*, 1997, **101**, 8141-8155.
42. S. Ito, P. Liska, P. Comte, R. L. Charvet, P. Pechy, U. Bach, L. Schmidt-Mende, S. M. Zakeeruddin, A. Kay, M. K. Nazeeruddin and M. Gratzel, *Chem. Commun.*, 2005, **34**, 4351-4353.
43. Q. Wang, J. E. Moser and M. Gratzel, *J. Phys. Chem. B*, 2005, **109**, 1 4945-14953.
44. C. Longo, A. Nogueira, M.-A. De Paoli and H. Cachet, *J. Phys. Chem. B*, 2002, **106**, 5925-5930.
45. Q. Wang, S. Ito and M. Gratzel, *J. Phys. Chem. B*, 2006, **110**, 25210-25221.
46. T. Hoshikawa, M. Yamada, R. Kikuchi and K. Eguchi, *J. Electrochem. Soc.*, 2005, **152**, E68-E73.
47. Y. Yoshida, S. Tokashiki, K. Kubota, R. Shiratuchi, Y. Yamaguchi, M. Kono and S. Hayase, *Sol. Energy Mater. Sol. Cells*, 2008, **92**, 646-650.
48. L. Han, N. Koide, Y. Chiba and T. Mitate, *Appl. Phys. Lett.*, 2004, **84**, 2433-2435.
49. M. Adachi, M. Sakamoto, J. Jiu, Y. Ogata and S. Isoda, *J. Phys. Chem. B*, 2006, **110**, 13872-13880.
50. R. Kern, R. Sastrawan, J. Ferber, R. Stangl, J. Luther, *Electrochim.Acta*, 2002, **47**, 4213-42

ToC

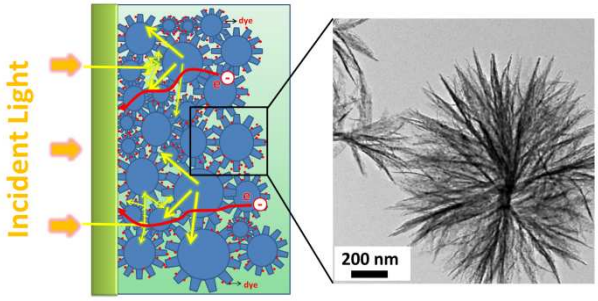

Highly connected hierarchical textured TiO_2 spheres, composed of high aspect-ratio nanosheets, gave high conversion efficiency in dye-sensitized solar cells.